Paper CIT06-593

OPTIMAL DESIGN OF A MICRO-SCALE VISCOUS PUMPS FOR MAXIMUM MASS FLOW RATE AND MINIMUM POWER CONSUMPTION – PRELIMINARY RESULTS

Alexandre K. da Silva
Department of Mechanical Engineering, University of Hawaii – Manoa, 2540 Dole St., Holmes Hall 302, Honolulu, HI 96822, USA
e-mail: akds@hawaii.edu

Marcelo H. Kobayashi
Department of Mechanical Engineering, University of Hawaii – Manoa, 2540 Dole St., Holmes Hall 302, Honolulu, HI 96822, USA
e-mail: marcelok@hawaii.edu

Carlos F. M. Coimbra
Department of Mechanical Engineering, University of Hawaii – Manoa, 2540 Dole St., Holmes Hall 302, Honolulu, HI 96822, USA
School of Engineering, University of California, P.O. Box 2039, Merced, CA 95344, USA
e-mail: coimbra@hawaii.edu

Abstract. *The present paper addresses the effect of geometric parameters such as channel height and rotor eccentricity on the mass flow rate and power consumption of a two dimensional micro-scale viscous pumps. The objective is to maximize the mass flow rate and at the same time minimize shaft power consumption when an external pressure load is applied along the channel that houses the rotor. Three different viscous micropump configurations were considered, a straight housed pump (I-shaped housing) and two curved housed pumps (L- and U-shaped housings). Because the performance of a micro viscous pumps are based on the asymmetric placement of the rotor within the surrounding housing, the numerical results show that the rotor eccentricity and the channel height have a major effect on the mass flow rate generated by the rotor and on the shaft power demanded by the rotor. Preliminary simulations showed that mass flow rate is maximized when the eccentricity is small. The results also show that micropumps with curved housing (i.e., L and U-shaped configurations) not only provide higher larger mass flow rates when compared with straight housed pumps, but also demand less shaft power to operate. Optimized geometric dimensions of all three configurations are presented for several values of the Reynolds number and pressure load.*

Keywords*. Viscous Pump, Optimal Design, Maximum Mass Flow Rate.*

1. Introduction

Advances in the miniaturization of electro mechanical systems have enabled the fabrication of microsystems or microelectromechanical systems (MEMS) that offer several advantages over conventional devices. These advantages include superior resolution, precision and sensitivity, lower costs, and reliability due to redundancy. In biological applications there is also the possibility of incorporating sensing, processing, and actuation nearby or on the same substrate – see the recent reviews on MEMS Judy (2001) and Ziaie *et al.* (2004). Because of their physical and engineering significance as well as the relevance of their applications, micropumps have figured prominently among the development of MEMS.

Micropumps, broadly defined as having dimensions smaller that 100 μm, have a myriad of applications ranging from single- or two-phase micro cooling devices for the thermal management of transient hot spots in microchips Qu and Mudawar (2002, 2003), to mass spectrometer systems and micropropulsion in space exploration Micci and Ketsdever (2000), to micro total analysis systems (μTAS) Reyes et al. (2002) and Auroux et al. (2002). Common to all these devices is the need to pump fluid at flow rates of up to 1000 milliliter per minute through dimensions of the micro or nano scales. Contrary to microelectronics that succeeded in scaling down its transistors and systems to provide faster and cheaper devices, pumping do not benefit from miniaturization in general. Indeed, ordinary inertia based devices, such as centrifugal pumps, do not work at the very low Reynolds number commonly associated with the micropumping requirements. This is due to the fact that, by its definition, at low Reynolds numbers inertia is small compared to the viscous force. Instead, effective micropumps belong to one of the following two main categories: the positive-displacement or reciprocating pumps and the dynamic or continuous flow pumps – see the recent reviews Nguyen (2002), Laser and Santiago (2004) and Woias (2004).

Typically, reciprocating micropumps use pulsating surface motion to displace the fluid by pressure work. By contrast, the physical-chemical and design principles involved in the continuous flow micropumps vary profusely. They include ultrasonic, electrohydrodynamic, electroosmotic, magnetohydrodynamic or electrochemical actuation. These micropumps do function but require sophisticated fabrication processes and involves complex sealing problems – see

the referred reviews for details. Sen et al. (1996) proposed a rotating micropump, where the relatively large viscous forces at these small scales are used to drive the fluid.

The viscous micropump combines the simplicity in design with effectiveness in pumping. Roughly speaking, the viscous micropump consists of a cylinder asymmetrically placed inside a micro-channel. When the cylinder rotates the difference in shear stresses on the lower and upper half of the cylinder creates a force imbalance that displaces the fluid. After its introduction in 1996, the viscous micropump has been the subject of a stream of publications including Sharatchandra et al. (1997), Sharatchandra et al. (1998), DeCourtye et al. (1998), Abdelgawad et al. (2004), Gad-el-Hak (1999) and Abdelgawad et al. (2005). These authors examined various design features and fundamentals issues associated with such micropumps, including the effects of channel height, rotor eccentricity and angular velocity on the pump performance Sen et al. (1996), slip velocity Sharatchandra et al. (1997), thermal effects Sharatchandra et al. (1998), transient effects Abdelgawad et al. (2004), and multistage configurations Abdelgawad et al. (2005). Yet none of these previous reports have considered the optimization of the mass flow constrained to shaft power consumption, which is a key factor in the design of efficient micropumps. Also, although extensive and detailed, all previous reports have worked with the original I-shaped house micropump.

In the present work we introduce a novel class of curved viscous micropumps with L- and U-shaped house pumps. For each of these house shapes we analyze the effect of the relevant parameters and study the optimum design for maximum mass flow rate at minimum power consumption. We start with a description of the micropump configuration and the numerical modeling in §2. In §3 we validate our numerical results by comparing our present results with the results reported by Sharatchandra et al. (1997) and Abdelgawad et al. (2004). With the validated model we proceed with the definition of the figure of merit and optimization procedure: §4 for unconstrained optimization and §6 constrained by shaft power. In §5 we report the unconstrained optimization of the various micropump shapes and in §7 we report the constrained optimum designs. In the last section §8 we sum up the main findings of this work.

2. Numerical Modeling

Consider the three micropump configurations shown in Fig. 1, where D represents the diameter of the rotor, L_u and L_d are the lengths of the upstream and downstream conduit channels, and H is the height of the conduit channel. Due to viscous diffusion, the clockwise-turning rotor impels the fluid from left to right against an imposed pressure difference $\Delta P = P_H - P_L$.

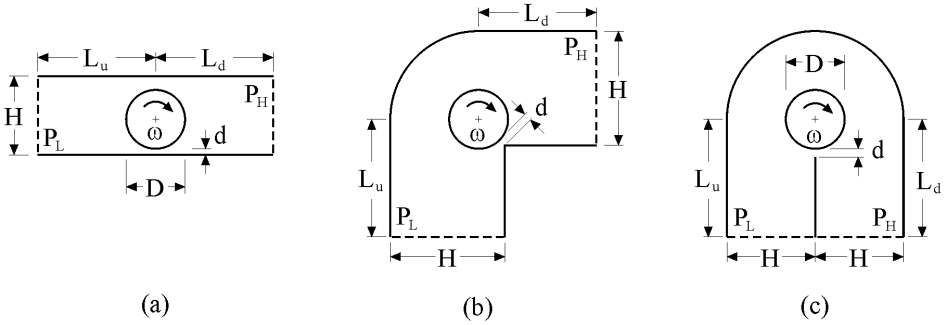

Figure 1. Numerical domain of a viscous micropump: (a) I-shaped channel, L-shaped channel and U-shaped channel.

The effectiveness of a viscous micropump is associated with the eccentricity of the rotor with respect to the surrounding walls. So we introduce a linear dimension d that indicates the distance between the lower wall and the rotor (see Fig. 1). For all three configurations, d = 0 means that the rotor touches the lower wall, not allowing any fluid flow between the lower wall and the rotor. If d > 0, the rotor does not touch the lower wall and fluid is allowed to flow between the rotor and the adjacent surfaces. Finally, d < 0 means that the rotor is partially embedded in the lower wall.Taking D as our length scale, the dimensionless geometrical parameters can be written as

$$(x, y, H, L_u, L_d, d)^* = (x, y, H, L_u, L_d, d)/D \tag{1}$$

The fluid is considered Newtonian with constant properties. Because of the slow character for the flow, no instabilities are expected and the flow is assumed steady, laminar and incompressible. We define the following dimensionless variables

$$(u, v)^* = (u, v)/(\omega D/2), \text{ and } P^* = (P_H - P_L)/(\rho v^2/D^2), \tag{2}$$

and write the governing equations as

$$\nabla \cdot \vec{V}^* = 0\,, \tag{3}$$

$$\mathrm{Re}_D^2 \, (\vec{V}^* \cdot \nabla) \vec{V}^* = - \nabla P^* + \mathrm{Re}_D \, \nabla^2 \vec{V}^* \ , \tag{4}$$

where $\mathrm{Re}_D = (\omega \, D^2/2 \, \nu)$ is the Reynolds number based on the rotor angular velocity and diameter. Due to the definition of the dimensionless pressure drop, Eq. (2), one should note that the pressure head the pump has to overcome is independent of the Reynolds number.

Three different viscous micropump configurations were considered: the standard straight or I-shaped pump, and two novel curved pumps: an L-shaped and a U-shaped. The numerical domain and the nomenclature are also shown in Fig. 1. The flow boundary conditions are: $P^* = P_L^* = 0$ at the inlet and $P^* = P_H^*$ at the exit plane, where $P_H^* = \Delta P^* - P_L^*$. The pressure boundary condition at the inlet and outlet is implemented as $\mathbf{n} \cdot \mathbf{T} = - P_L$ at the inlet and $\mathbf{n} \cdot \mathbf{T} = - P_H$ at the outlet, where $\mathbf{T} = \sigma \mathbf{n}$ is the stress vector and σ is the Stokes stress tensor $\sigma = - P\mathbf{I} + \nu \, (\nabla \mathbf{u} + \nabla \mathbf{u}^T)$. In addition, the tangential components of the velocities are set to zero (i.e., $\mathbf{t} \cdot \mathbf{u} = 0$) at the inlet and outlet of the micropump. Non-slip velocity conditions were used in all internal surfaces of the channel. The velocity of the rotor surface is maintained constant at $U = \omega \, D/2$ for each run. We adopted zero tangential velocities at the inlet and outlet after many numerical tests indicated that fully developed flow conditions at the inlet and outlet were obtained for values of L_u and L_d greater than 4D. In all numerical simulations we take L_u and L_d to be 8D each. It is important to mention that in the case of a U-shaped micro viscous pump (i.e., Fig. 1c), a small gap with a dimensionless length equal to 0.025, was imposed between the inner vertical walls of the inlet and outlet channel located below the rotor. This adaptation was necessary due to the fact the micropump housing was not include in the numerical domain.

Our numerical simulations were performed using the Finite Elements Method toolbox COMSOL Multiphysics®, v. 3.2 from COMSOL, Inc. Second and first order Lagrange p2-p1 mixed finite-elements were used to stabilize the pressure (i.e., 2nd order Lagrange elements to model velocity and linear Lagrange elements for the pressure). The mesh density was exhaustively tested in order to guarantee that the results were mesh-independent. Table 1 exemplifies the mesh convergence of two figures of merit: dimensionless average flow velocity ($\overline{u}^*$) and dimensionless shaft power (W'^*/Re_D^2), which are defined later in the text (§ 3 and 7), for an I-shaped viscous micropump. According to Table 1, the ideal mesh density for the average flow velocity is obtained relatively fast when compared with the mesh density needed for the evaluation of the shaft power, which, through the shear stresses, involves the derivatives of the velocity at the surface of the rotor. For all three configurations, the optimal number of elements is between 10,000 and 15,000, which are distributed unevenly through the numerical domain, with a denser mesh being used in the neighborhood of the rotor. When the computation of the group W'^*/Re_D^2 is required (i.e., Figs. 10-13), an even higher concentration of elements was used around the rotor, which increases the total number of elements to over 20,000 on average, depending on the channel height.

Table 1. Fig. 1a, $\mathrm{Re}_D = \Delta P^* = 1$, $H^*=1.5$ and $d^* = 0.6$.

Number of elements	$\overline{u}^*$	$\left\|(\overline{u}_i^* - \overline{u}_{i+1}^*)/\overline{u}_i^*\right\| \times 10^2$	W'^*/Re_D^2	$\left\|(W'^*_i - W'^*_{i+1})/W'^*_i\right\| \times 10^2$
109	0.073923	< 0.1 %	33.96356	-
436	0.073908	< 0.1 %	31.12104	-
1744	0.073882	< 0.1 %	26.69661	14 %
3486	0.073878	< 0.1 %	25.67958	3.8 %
11216	0.073877	< 0.1 %	25.25148	1.6 %
28662	0.073878	< 0.1 %	25.05145	0.8 %

The solution was obtained with a stationary, non-linear solver based on a damped Newton's Method. The relative error convergence criterion is the weighted Euclidian norm defined as

$$\mathrm{err} = \left[\frac{1}{N} \sum_i \left(\frac{|E_i|}{W_i} \right)^2 \right]^{1/2} \tag{5}$$

where N is the number of degrees of freedom, $\mathbf{E}_i = \mathbf{U}_i - \mathbf{U}_{i-1}$ is the estimated error of the current solution vector $\mathbf{U}_i$ and $W_i = \max(|\mathbf{U}_i|, \mathbf{S}_i)$ are the weighted factors. The $\mathbf{S}_i$ factor is defined as the product of a constant, in this case 0.1, times the average of all $|\mathbf{U}_j|$ for all the degrees of freedom. The damping factor was set initially equal to 10^{-4} and the convergence criterion was set equal to 10^{-6}.

3. Validation of the Method

First, we validate our numerical code for this application against previous results obtained by Sharatchandra et al. (1997) and Abdelgawad et al. (2004). Table 2 compares the effect of the imposed pressure load on the average fluid

velocity ($\bar{u}^*$) at the exit plane between the present results and the results obtained by Sharatchandra et al. (1997), considering $Re_D = 1$, $H^*=1.5$ and $d^* = d^*_{max} = 0.025$, where the average fluid velocity is defined as

$$\bar{u}=H^{-1}\int_0^H u(y)dy\,, \tag{6}$$

and d^*_{max} stands for the minimal distance between the rotor and the lower wall considered by Sharatchandra et al. (1997) in their numerical calculations. In the present work d^*_{max} is set equal to 0.025.
According to Table 2, an acceptable overall agreement with previous results is achieved with an average difference of the order of 1% throughout the relevant range of ΔP^*. Table 3 validates our code for a configuration in which the parameters Re_D, ΔP^* and ε_{mod} are held fixed at 1, 1 and 0.25 respectively, and H^* varies as indicated. ε_{mod} is the modified eccentricity of the rotor defined by Sharatchandra et al. (1997) as

$$\varepsilon_{mod} = 0.5(H - D - d)/D = 0.5(H^* - 1) - d^*\,, \tag{7}$$

where d^* is the dimensionless distance between the rotor and the lower wall shown in Fig. (1). One should notice that, Table. 3 not only shows a good agreement between our results and the data obtained by Sharatchandra et al. (1997), but also, shows the detrimental effect of the channel height (H^*) on the overall performance of the pump for a fixed value of $\varepsilon_{mod} = 0.25$. According to Eq. 7, the larger the channel height (H^*), the closer the rotor is to the centerline of the channel if ε_{mod} is held fixed. In other words, the gap d^* increases with H^*, which in turn reduces the average fluid velocity.

Table 2. Validation of the numerical results for: Fig. 1a, $Re_D= 1$, $H^*=1.5$ and $d^* = d^*_{max} = 0.025$.

ΔP^*	$\bar{u}^*$ Present Work	$\bar{u}^*$ Sharatchandra et al. (1997)	Difference %
0	0.105789	0.106	0.2
7.5	0.074099	0.075	1.2
1.5	0.042410	0.043	1.4
22.5	0.010702	0.011	2.8
30	–0.020967	–0.021	0.16

Table 3. Validation of the numerical results for: Fig. 1a, $Re_D= 1$, $\Delta P^* =1$, and $\varepsilon_{mod} = 0.25$.

H^*	$\bar{u}^*$ Present Work	$\bar{u}^*$ Sharatchandra et al. (1997)	Difference %
1.5	0.101568	0.102	0.42
2	0.055956	0.057	1.8
2.5	0.026987	0.027	0.05

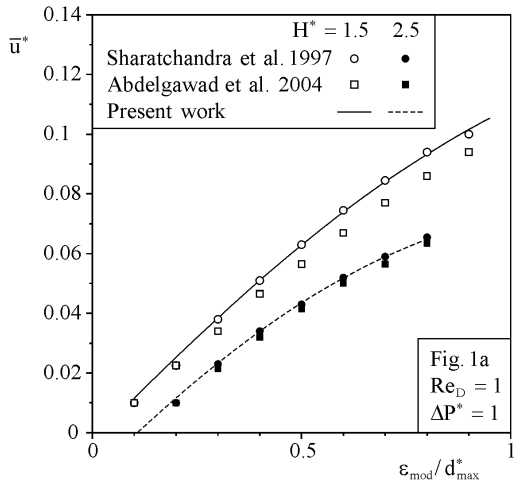

Figure 2. Code validation.

To conclude the code validation, the effect of a third parameter ($\varepsilon_{mod}/d^*_{max}$) on the average fluid velocity is considered. Figure 2 shows the direct comparison between the data obtained in present study and the results from Sharatchandra et al. (1997) and Abdelgawad et al. (2004) for an I-shaped viscous micropump operating with Re_D =

$\Delta P^* = 1$, and two values of the channel thickness: $H^* = 1.5$ and 2.5. According to Fig. 2 a nearly prefect agreement between our results and the results of Sharatchandra et al. (1997) is obtained.

4. Optimization Goal

As previously stated, the present study has two main objectives: to determine the optimal geometrical parameters (i.e., channels thickness H^* and rotor/wall gap d^*) that result in maximum mass flow rate ($\dot{m}^*$), and to study the performance of our newly proposed L- and U-shaped micropumps when compared with the traditional I-shaped design pioneered by Sen et al. (1996). The mass flow rate per unit of length is defined as

$$\dot{m}^* = \bar{u}^* H^* . \tag{8}$$

In the first round of optimization (Figs. 2-9), no constraints were considered and the optimal geometric dimensions (i.e., channels thickness H^* and rotor gap d^*) were determined based on parameters such as Re_D and ΔP^*. In this scenario, the optimization opportunity emerges from the fact that a viscous micropump operates based on two main conditions: the need of a certain level of confinement (i.e., a finite value for H^*), and the asymmetric placement of the rotor inside the channel. The need for the first condition can be understood by noticing that, in the limit where $H^* >> (1 + d^*)$, the fluid average velocity tends to zero ($\bar{u}^* \rightarrow 0$). Consequently, the mass flow rate also tends to zero since $\dot{m}^* \sim \bar{u}^*$. In the other limit of 'small' values of the dimensionless channel thickness (i.e., $H^* \rightarrow (1 + d^*)$), it is clear that the flow is constricted between the rotor and the upper wall of the pump's channel, which also reduces the mass flow rate. Based on the above, an optimal value for H^* such that $\dot{m}$ is maximized must exist.

The need for the rotor asymmetry to displace the fluid in a viscous micropump can be understood by analyzing limiting cases of asymmetry. Consider, for instance, an I-shaped micropump with no pressure load across the channel. Assuming that the rotor is located in the center of the channel, zero net flow is obtained, regardless the direction in which the rotor spins. However, if the symmetry is broken as a clockwise spinning rotor approaches the upper wall, a net flow from the right to the left is generated. In this case, the symmetry break provides a preferential direction for the net flow due to the increase in the shear between the fluid and the surrounding walls. On the other hand, the rotor asymmetry increases the shaft power requirement due to proximity of the rotor to the closest wall. The effect of parameters such as Re_D, ΔP^*, H^* and d^* on the shaft power demand will be addressed later in the text in §6 and §7.

5. Unconstrained Optimization

The search for the optimal geometrical configuration started with the simplest design possible, Fig. 1a. In this case, we have two degrees of freedom, the channel thickness H^* and the gap d^*. Assuming fixed values for d^*, Re_D and ΔP^*, we were able to find an optimal value for the channel height H^* that maximizes the average flow velocity ($\bar{u}^*$) and the mass flow rate ($\dot{m}^*$) just by varying H^*. Figure 3 shows that the channel thickness has a strong effect on $\bar{u}^*$ and $\dot{m}^*$, which strengthens the need for optimizing geometric parameters in a viscous micropump. Figure 3 also shows that different values of the optimal channel height (H^*_{opt}) are needed to maximize $\bar{u}^*$ and $\dot{m}^*$.

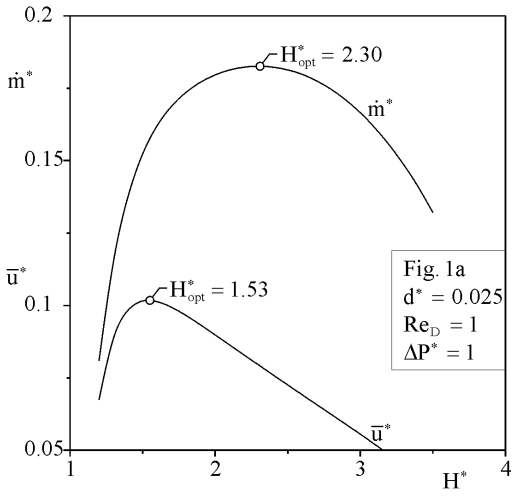

Figure 3. Effect of the channel spacing (H^*) on the mean flow velocity and mass flow rate for an I-shaped channel.

Figure 4 shows the effect of the rotor gap on the mass flow rate and average fluid velocity for an I-shaped pump with the following operating conditions: $Re_D = \Delta P^* = 1$. Each one of the open symbols shown in Fig. 4 represents the

maximum value of $\dot{m}^*$ (squares) and $\overline{u}$ (circles) that can be obtained for a given value of d^*. That is, implicit in each symbol, is the optimization of $\dot{m}^*$ and $\overline{u}^*$ with respect to the channel thickness H^*, which is shown later in Fig. 5. According to Fig. 4, the maximum values of $\dot{m}^*$ and $\overline{u}^*$ are found around $d^*_{opt} \sim 0$, which represent the maximum mass flow rate and average flow velocity optimized with respect to two degrees of freedom, d^* and H^*. Figure 4 also reveals that the gap d^* plays a major role on $\dot{m}^*$ if $d^* \neq d^*_{opt}$ (i.e., $d^* > d^*_{opt}$), similarly to Fig. 3, where values of H^* larger or smaller than H^*_{opt} were equally detrimental to our two figures of merit (i.e., $\dot{m}^*$ and $\overline{u}^*$). On the other hand, Fig. 4 shows that it maybe desirable to have $d^* < d^*_{opt}$ (i.e., the rotor partially embedded in the lower wall) due to the weak effect of the negative eccentricities on the average flow velocity.

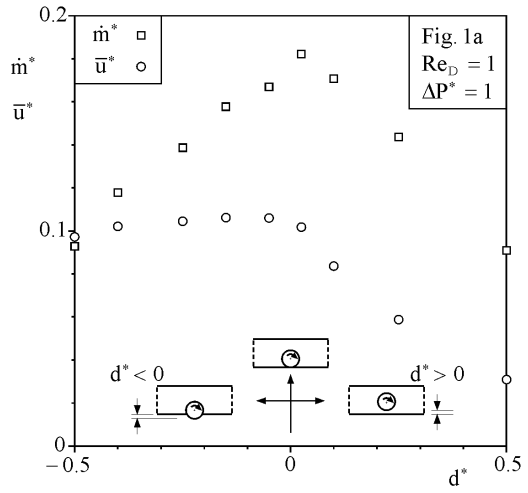

Figure 4. Effect of the rotor gap (d^*) on the maximal mass flow rate and mean velocity.

Figure 5 shows the effect of the gap d^* on the optimal channel height H^*_{opt}. According to Fig. 5, H^*_{opt} increases monotonically with d^*. This behavior can be explained by the fact that, because viscous micropumps need the rotor to be asymmetrically placed inside the channel (§ 5), any increment in d^* is associated with an increment in H^*_{opt} to ensure asymmetry.

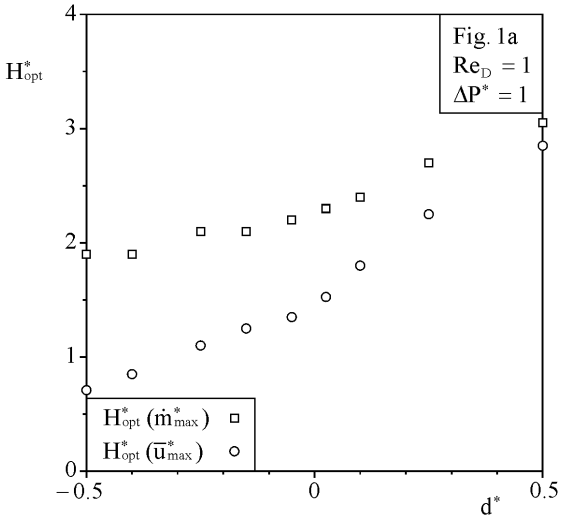

Figure 5. Optimal channel thickness for a fixed value of d^*.

Figure 6 shows the optimal channel thickness versus the Reynolds number for the three configurations given in Fig.1. In order to reduce the number of computational runs, we factored in the results presented in Fig. 4, which showed that $d^*_{opt} \sim 0$. In all simulation shown in Fig. 6, d^* was held constant and equal to 0.025. Figure 6 shows that the optimal channel thickness increases with Re_D for all the configurations. Additionally, a transition between the relative magnitude of H^*_{opt} for the I-, L- and U-shaped pumps can be identified at $Re_D \sim 0.2$. For values of the Reynolds number between $0.01 < Re_D < 0.1$, $H^*_{opt,\,Fig.\,1a} > H^*_{opt,\,Fig.\,1b} > H^*_{opt,\,Fig.\,1c}$. For values the Reynolds number between $0.3 < Re_D < 1$, $H^*_{opt,\,Fig.\,1c} < H^*_{opt,\,Fig.\,1b} > H^*_{opt,\,Fig.\,1a}$. The importance of such results lies in the need for compact micropumps, due to the limited space available to house the micropump itself. In this case, the space occupied by the micropump has to respect

area constraints, which make L-shaped and U-shaped micropumps more attractive when $Re_D < 0.2$ and I-shaped pumps more compact in the limit where $Re_D > 0.2$.

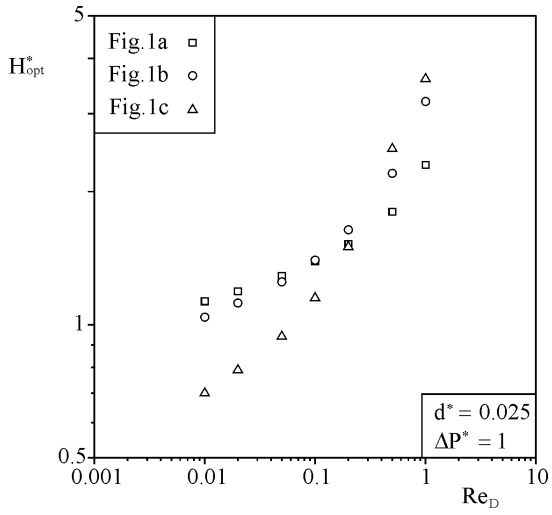

Figure 6. Effect of the Reynolds number on the H^*_{opt} for the three viscous micropumps given in Fig. 1.

Figure 7 depicts the effect of the micropump configuration (Fig. 1a-c) on the figure of merit ($\dot{m}^*_{max}$) for several values of the Reynolds number. According to Fig. 7, pumps with curved housing (i.e., L and U-shaped micropump) perform better (i.e., present higher values of $\dot{m}^*_{max}$) than the I-shaped pump, especially for higher values of the Reynolds number. One reasonable explanation for the latter is that, in the pumps with curve housing the fluid is more aligned to the rotor. This is an important result that extends the applicability of viscous micropump to higher mass flow rates, making it even more attractive when compared with other micropumping methods (see §1).

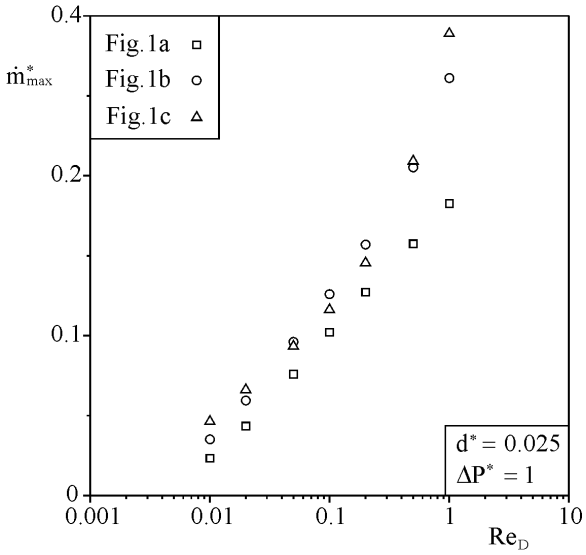

Figure 7. Direct comparison between the maximum mass flow rate ($\dot{m}^*_{max}$) of the three micropumps given in Fig. 1.

Figure 8a shows the effect of the pressure load (ΔP^*) on the optimal channel spacing H^*_{opt} assuming that $Re_D = 1$ and $d^* = 0.025$. According to Fig. 8a, the optimal channel thickness decreases as ΔP^* increases for the three configurations of Fig. 1. Also, a transition between the thickness of the channel housing of the pump can be observed for pressure loads between $5 < \Delta P^* < 10$. In the limit where $\Delta P^* < 5$, pumps with curved housing require larger values of H^*_{opt} when compared with an I-shaped pumps. Figure 8a also suggest that, in the limit where $\Delta P^* > 10$, I-shaped pumps demands a larger channel thickness than curved housed pumps (Fig. 1b and c).

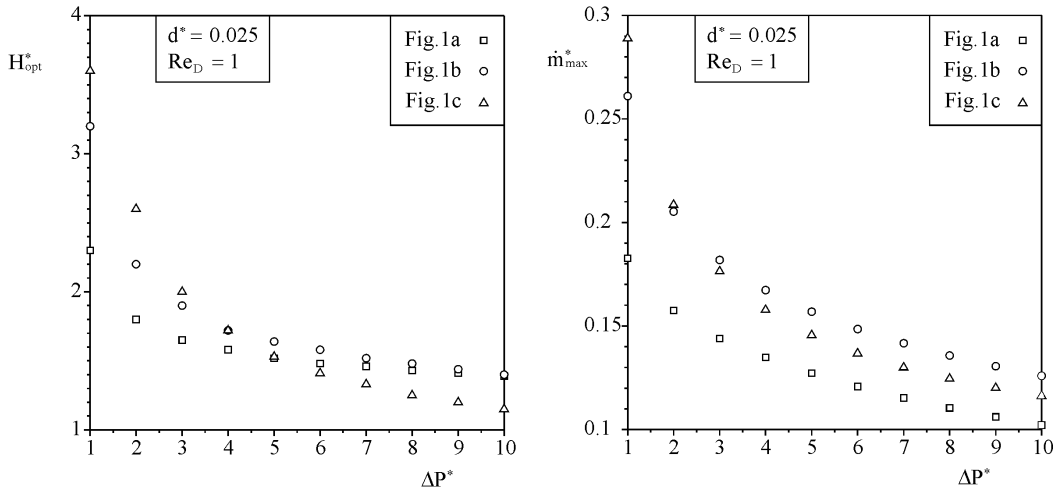

Figure 8. a) Effect of the counter pressure (ΔP^*) on the optimal channel thickness H^*_{max} (left frame). b) Effect of the counter pressure (ΔP^*) on the maximum mass flow rate $\dot{m}^*_{max}$ (right frame).

Figure 8b depicts the importance of the use of pumps with curved housing (Figs. 1b and 1c) when the objective is to maximize the mass flow rate at larger pressure loads. Figure 8b shows that the L and U-shaped pumps present superior performance when compared with an I-shaped throughout the range of load pressure $1 < \Delta P^* < 10$. Also, as expected, the maximized mass flow rate decrease significantly as ΔP^* increases.

6. Minimization of the Shaft Power

Thus far, we have studied the performance and optimization of viscous micropumps with curved or otherwise houses without constraints on the shaft power (See Figs. 7 and 8b). Yet subjacent to these results lays an important question on how does the pump housing, Reynolds number, load pressure and geometric parameters (e.g., d^*, H^*_{opt}) affect the shaft power requirements? To answer this question, we start by defining the rotor's moment coefficient as

$$M = -\int_0^{2\pi} \tau \, d\theta \, . \tag{9}$$

Knowing that the torque per unit of length applied to rotor is $T' = M\, 2\pi\, R^2$ and that shaft power per unit of length is $W' = T\, \omega$, one can define the dimensionless shaft power per unit of length applied at the rotor as

$$W'^* = M^*\, Re_D^2 \, . \tag{10}$$

Intuitively, the shaft power (W'^*) required by the rotor increases with Re_D and also as $d^* \to 0$. That's because higher values of Re_D and small gaps between the walls of the channel surrounding the pump and the rotor increase friction. Such observation is in agreement with Eq. 10, where one can learn that the dimensionless shaft power per unit of length applied to the rotor varies linearly with M^*, and with the square power of the Reynolds number. It is clear that, embedded in the value of M^*, are the geometrical parameters of the pump, such as the rotor gap and channel height.

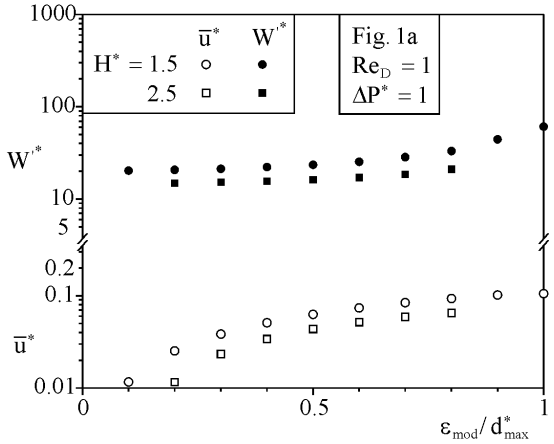

Figure 9. Effect of the modified gap (d^*) on the rotor's shaft power (W'^*).

Our numerical results for the dimensionless shaft power were validated with the numerical data obtained by Abdelgawada et al. (1997) in the steady state limit, since they performed a transient analysis. One should note that the eccentricity in Tables 4 and 5 follows the definition used in Abdelgawada et al. (1997), where

$$\varepsilon_{mod,1} = 1 - 2d^* / (H^* - 1) . \tag{11}$$

Tables 4 and 5 show a good agreement between both set of results.

Table 4. Validation of the numerical results for: Fig. 1a, Re_D= 1, ΔP^* =0, and $\varepsilon_{mod,\,1}$ = 0.95.

H^*	W'^* Present Work	W'^* Abdelgawada et al. (1997)	Difference %
1.5	59.68	~ 60.0	0.5
2.5	35.82	~ 35.9	0.2
3.5	28.49	~ 29.1	1.7

Table 5. Validation of the numerical results for: Fig. 1a, Re_D= 1, ΔP^* = 0, and H^* = 1.5.

$\varepsilon_{mod,\,1}$	W'^* Present Work	W'^* Abdelgawada et al. (1997)	Difference %
0.2	20.69	~ 20.6	0.4
0.8	33.05	~ 34.2	3.5
0.95	59.69	~ 60.1	0.7

Figure 9 shows the effect of the group $\varepsilon_{mod}/d^*_{max}$ on the rotor shaft power demanded (solid symbols) by an I-shaped pump with two different values of channel height, H^* = 1.5 and 2.5, and operating with the following conditions: Re_D = ΔP^* = 1. According to Fig. 9, W'^* increases with the rotor confinement (i.e., W'^* (H^* =1.5) > W'^* (H^* =2.5)). This is an interesting result that allows us to question the superior performance of the pump with small channel height, since it demands more power.

Also, one should notice that, the apparently missing symbols (squares) in Fig. 9 for the curves in which H^* = 2.5, is due to the fact that when the group $\varepsilon_{mod}/d^*_{max}$ < 0.2, the average fluid velocity becomes too small since the rotor is moving towards the channel center line. In the other limit where $\varepsilon_{mod}/d^*_{max}$ > 0.8, the gap between the rotor and the lower wall becomes d^* < 0.05, which also .

Figure 10 compares the effect of the load pressure (ΔP^*) and micropump configurations (Fig. 1a-c) on the shaft power demand W'^*. The three sequences of symbols represent the shaft power needed such that the micropump returns the maximum value of mass flow as indicated in Fig. 9, considering Re_D = 1 and when d^* = 0.025. At first, one should note that the pressure load has a minor effect on W'^*, regardless the housing configuration, since all three curves are nearly flat. However, more important is to realize that curved housed pumps (Fig. 1b and c) not only provide higher mass flow rate (see Fig. 8b) when compared with the I-shaped configuration of Fig. 1a, but also, they require much less shaft power as shown in Fig. 10. The combination of the results provided by Figs. 8b and 10, clearly shows the superiority of the micropump with curved housing, as compared with I-shaped micropumps.

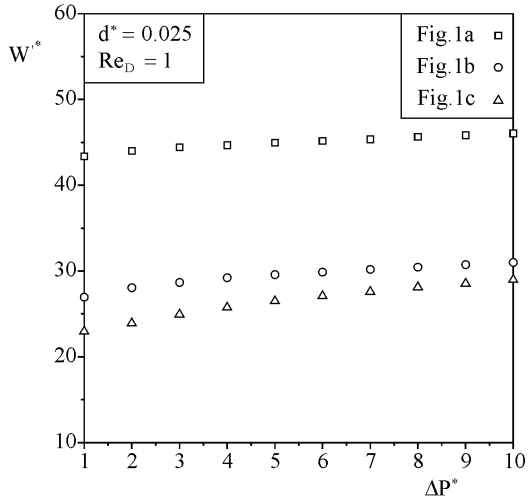

Figure 10. Effect of the counter pressure (ΔP^*) on the rotor's shaft power (W'^*).

Figure 11 further supports the choice of curved housed micropumps in a wider range of the Reynolds number, $0.01 < Re_D < 1$. To better understand why, we have to analyze Fig. 11 in conjunction with Fig.7, which shows that higher mass flow rates are provided by curved housed micropump throughout the whole range $0.01 < Re_D < 1$ in comparison with an I-shaped micropump. In this context, Fig. 11 corroborates our conclusions that configurations with curved housing also require less power to operate.

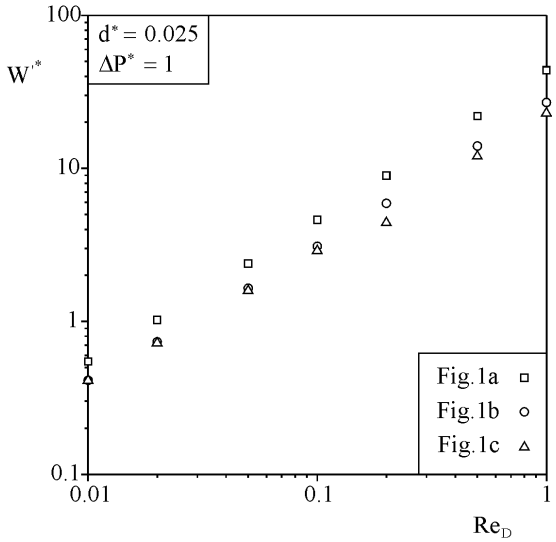

Figure 11. Effect of the Reynolds number on the rotor's shaft power (W'^*).

7. Constrained Rotor's Shaft Power

Our numerical experiments showed that the rotor of a viscous micropump needs to be placed asymmetrically inside the conduit channel in order to generate a net flow, and, as shown in Figs. 4 and 7, the mass flow rate increases with Re_D and when $d^* \rightarrow 0$. Therefore, the micropump designer, who has a limited amount of shaft power available, is entitled to ask the following question: assuming that the rotor's shaft power is constrained, is it better in terms of maximizing the mass flow rate to have the rotor turning faster (i.e., higher values of Re_D) or to place the rotor closer the channel's wall in order to increase the asymmetry level such that $d^* \sim 0$? The optimization opportunity emerges from the need of maximum mass flow and least shaft power.

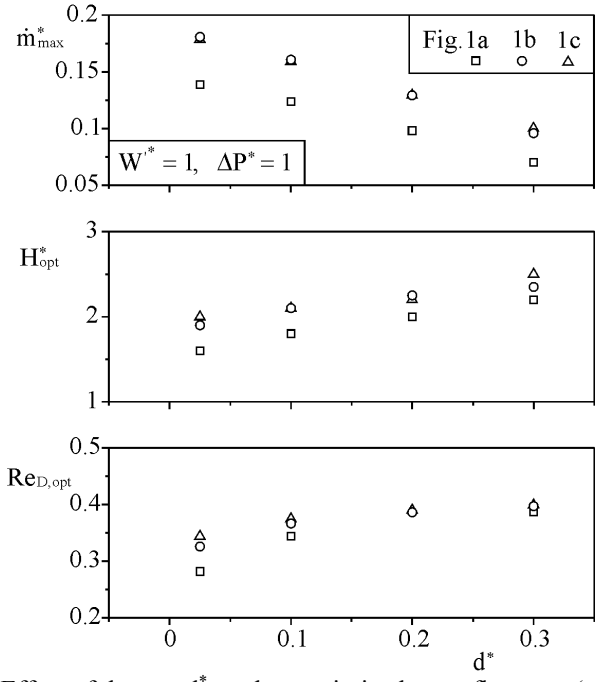

Figure 12. Effect of the gap d^* on the maximized mass flow rate (upper frame), optimal channel height (middle frame) and, optimal Reynolds number (lower frame) assuming that the shaft power is fixed and equal to 10.

In order to answer the previous question, numerical simulations were conducted for the three configurations given in Fig. 1 aiming at the determination of the optimal values of the channel height (H^*_{opt}) and the optimal rotor speed, here represented by the Reynolds number ($Re_{D,opt}$), such that a given (fixed) shaft power availability is respected through Eq. 10. In this case, the available shaft power and the pressure load were set equal to 1. One should notice that $\dot{m}^*_{max}$ represents the maximum mass flow rate obtained for a given value of d^*. However, because the dimensionless shaft power was set equal to $W'^* = 1$, each symbol shown in the Fig. 12 originates from the maximization of $\dot{m}^*_{max}$ with respect to two degrees of freedom, the channel height (H^*) and the rotor speed (i.e., $Re_{D,opt}$). According to the upper frame of Fig. 12, the superior performance of curved housed pumps is evident when compared with an I-shaped configuration since $\dot{m}^*_{max,Figs.1b}$ and $\dot{m}^*_{max,Figs.1c}$ are larger than $\dot{m}^*_{max,Figs.1a}$. Also interesting is that the maximized mass flow rate decreases as gap d^* increases. This result answers the question posed at the first paragraph of the current section, by showing that it is desirable to have the rotor closer to the bottom wall with lower angular speed, rather than have the rotor away from the bottom wall with a larger angular velocity ω. The middle frame of Fig. 12 shows that H^*_{opt} increases with d^* and that micro-scale viscous pumps with curved housing require slightly larger H^*'s when compared I-shaped pump. The increase of H^*_{opt} with d^* is explained based on the two main factors, the need for an asymmetric placement of the rotor within the surrounding walls, and the increase of $Re_{D,opt}$ with d^* (lower frame of Fig. 12), which is an indication that the friction is reduced as the rotor is moved away from the lower wall.

8. Conclusions

In this paper we use a FEM code to simulate and optimize the performance of a micro-scale viscous pump. The objective is to show the importance of geometric optimization on the mass flow rate and power consumption of a micro-scale viscous pump. In the first part of the paper, §5, we illustrated the effect of four parameters (i.e., rotor eccentricity and speed, height of the housing channel height and pressure load) on the performance of an I-housed micro-scale viscous pump proposed by Sen et al. (1996). The numerical results showed that the channel height (H^*) and the rotor eccentricity have a major effect on $\dot{m}^*$ and that geometric optimization of the pump's housing should be considered. At the end, optimized configurations (i.e., H^*_{opt} and ε^*_{opt}) based on maximization of the mass flow rate were generated.

Next, two new configurations of pumps with curved housing (Figs. 1b and 1c) were proposed and numerically optimized for maximal mass flow rate. The numerical results showed that pump with curved housing provide larger mass flow rates when compared with straight housed pumps (Fig. 1a) throughout a whole range of Reynolds number ($0.01 < Re_D < 1$) and pressure load ($1 < \Delta P^* < 10$). Furthermore, the results showed that curved housed pumps also require less shaft power to operate, which is an interesting feature for devices with limited power supply (i.e., laptops etc).

In §7, we reported the performance of all three configurations of Fig. 1 under global constraints. In this case, we fixed the amount of shaft power (W'^*) available to the rotor and varied the geometric parameters (H^* and d^*) and the rotor angular speed (Re_D). The most important finding is that curved housed pumps provided larger mass flow rates than an I-shaped pump. Also interesting is that, because the friction on the rotor surface decreases as the gap increases, the optimal Reynolds number increases with the gap. However, this combination of effects (larger Re_D and large gap) is not enough to guarantee the steadiness of the maximized mass flow rate, and because of that any increase in the rotor gap (d^*) has a detrimental effect on the maximized mass flow rate. In summary, if W'^* is fixed, it is desirable to have a configuration where the rotor is closer to the bottom wall (i.e., small gap) with a lower angular velocity, than a configuration with large d^* and a larger angular velocity.

Nomenclature

d	rotor distance from lower wall, m
D	rotor diameter, m
H	channel height, m
L	channel length, m
$\dot{m}$	mass flow rate, $kg\,s^{-1}$
M	moment coefficient, $N\,m^{-2}$
P	pressure, $N\,m^{-2}$
Re_D	Reynolds number, ($Re_D = \omega D^2/2\nu$)
T	torque, N m
U	rotor surface velocity, $m\,s^{-1}$
$\bar{u}$	mean velocity, $m\,s^{-1}$
$\bar{V}$	velocity vector, $m\,s^{-1}$
W'	rotor shaft power per unit of length, $N\,s^{-1}$

Greek Symbols

ε_{mod}	modified eccentricity, Eq. 7

$\varepsilon_{mod,\,1}$ modified eccentricity, Eq. 11
ν kinematic viscosity, $m^2\,s^{-1}$
ρ density, $kg\,m^{-3}$
ω rotor angular velocity, ($\omega = 2U/D$)

Subscripts

d downstream
H high
L low
max maximum
opt optimum
u upstream

Superscript

* dimensionless variables

Acknowledgement

A. K. da Silva thanks the College of Engineering of the University of Hawaii - Manoa for the support through a 2006 CoE Seed-Grant Award.

References

Abdelgawad, M., Hassan, I., Esmail, N., 2004. Transient behavior of the viscous micropump. Microscale Thermophysical Engineering **8**, 361-381.

Abdelgawad, M., Hassan, I., Esmail, N., Phutthavong, P., 2005. Numerical investigation of multistage viscous micropump configurations. Journal of Fluids Engineering **127**, 734-742.

Auroux, P.-A., Iossifidis, D., Reyes, D. R., Manz, A., 2002. Micro Total Analysis Systems. 2. Analytical standard operations and applications. Analytical Chemistry **74,** 2637 – 2652.

Blanchard, D. B., Ligrani, P. M., Gale, B. K., 2004. Single-disk and double-disk viscous micropump. International Mechanical Engineering Congress, paper # 61705.

COMSOL MultiPhysics Inc., (2005). User's Manual, Los Angeles, CA 90024.

DeCourtye, D., Sen, M., Gad-el-Hak, M. 1998. Analysis of Viscous Micropumps and Microturbines. International Journal of Computational Fluid Dynamics **10, 1**3 – 25.

Gad-el-Hak, M., 1999. The fluids mechanics of microdevices – The Freeman Scholar Lecture. Journal of Fluids Engineering **121**, 5-33.

Judy, J. W., 2001 Microelectromechanical systems (MEMS): fabrication, design and applications. Journal of Smart Materials and Structures **10,** 1115 – 1134.

Laser, D. J., Santiago, J. G., 2004. A review of micropumps. Journal of Micromechanics and Microengineering **14,** R35 – R64.

Micci, M. M., Ketsdever, A. D., 2000. Micropropulsion for Small Spacecraft. American Institute of Aeronautics and Astronautics Inc., Reston, Va., 399 – 422.

Nguyen, N.-T., Huang, X., Chuan, T. K., 2002. MEMS-Micropumps: a review. Journal of Fluids Engineering **124,** 384 – 392.

Qu, W., Mudawar, I., 2002. Experimental and Numerical Study of Pressure Drop and Heat Transfer in a Single-Phase Micro-Channel Heat Sink. International Journal of Heat and Mass Transfer **45,** 2549 – 2565.

Qu, W., Mudawar, I., 2003. Thermal Design Methodology for High-Heat-Flux Single-Phase and Two-Phase Micro-Channel Heat Sinks. IEEE Transactions on Components and Packaging Technologies **26,** 598 – 609.

Reyes, D. R., Iossifidis, D., Auroux, P.-A., Manz, A., 2002. Micro Total Analysis Systems. 1. Introduction, theory, and technology. Analytical Chemistry **74,** 2623 – 2636.

Sen, M., Wajerski, D., Gad-el-Hak, M. 1996. A novel pump for MEMS applications. Journal of Fluids Engineering **118**, 624-627.

Sharatchandra, M. C., Sen, M., Gad-el-Hak, M., 1997. Navier-Stokes simulations of a novel viscous pump. Journal of Fluids Engineering **119**, 372-382.

Sharatchandra, M. C., Sen, M., Gad-el-Hak, M., 1998. Thermal aspects of a novel viscous pump. Journal of Heat Transfer **120,** 99 – 107.

Ziaie, B., Baldi, A., Lei, M., Gu, Y, Siegel, R. A., 2004. Hard and soft micromachining for BioMEMS: review of techniques and examples of applications in microfluidics and drug delivery. Advanced Drug Delivery Reviews **56,** 145 – 172.

Woias, P., 2004. Micropumps – past, progress and future prospects. Sensors and Actuators B **105,** 28 – 38.